ADVANCED FUNCTIONAL MATERIALS
www.afm-journal.de

Enhancing the Efficiency of Indoor Perovskite Solar Cells through Surface Defect Passivation with Coplanar Heteroacene Cored A–D–A-type Molecules

Bing-Huang Jiang, Zhen-Jie Gao, Chien-Yu Lung, Zhong-En Shi, He-Yun Du, Yu-Wei Su, Hui-Shan Shih, Kun-Mu Lee, Hsin-Huai Hung, Choon Kit Chan, Chih-Ping Chen, and Ken-Tsung Wong**

The passivation of perovskite interfacial defects by the electron transport layer (ETL) has emerged as an effective strategy for enhancing the performance of perovskite solar cells (PSCs). Dithieno[2,3-d:2′,3′-d′]thieno[3,2-b:3′,2′-b′]dipyrrole (DTPT)-based acceptor-donor-acceptor (A–D–A) molecules composed of coplanar heteroacene as electron-donating core end-capped with various electron-accepting moieties are designed and examined as ETL modifiers for PSCs. Employing PCBM:DTPTCY as the ETL results in passivation perovskite defects, facilitation energy alignment at the ETL/perovskite interface, and enhancement of carrier transport efficiency. The optimized blended ETL-based $Cs_{0.18}FA_{0.82}Pb(I_{0.8}Br_{0.2})_3$ p-i-n PSC exhibit performances of 37.2% and 39.9% under TL84 and 3000K LED (1000 lux), respectively. The DTPTCY-based device demonstrates remarkable stability, retaining 87% of its initial power conversion efficiency (PCE) after 30 days of storage in a 40% relative humidity (RH) ambient air environment without any encapsulation, surpassing the control device, which retains only 67% of its original PCE. These findings underscore the potential of A–D–A-type molecule-based interface modification to enhance passivation and contact properties, ultimately leading to high-efficiency and stable PSCs.

1. Introduction

The energy consumption for "Internet of Things" (IoT) (i.e integration of sensors, telecommunications, remote actuators, smart devices) is a rising demand that requires constant and sustainable energy sources.[1] Self-powered integrated IoT devices by harvesting energy from indoor photovoltaics (iPVs) have obtained significant attention. Among the PV technologies, the organometal lead halide perovskite solar cells (PSCs) with high performance (>26% at 1 sun (100 mW cm^{-2} AM 1.5 G)) and easily controlled energy bandgap (E_g) via compositional engineering have great potential for use under indoor light sources inside buildings.[2] Because of these advantages, perovskites can highly meet most of the indoor light spectrum (e.g., fluorescent lamp (FL) or light emitting diode (LED), etc.) for the emerging high-performance iPV.[2c,3]

Traditionally, the optimal E_g for perovskite materials used in iPVs falls within

B.-H. Jiang, C.-Y. Lung, Z.-E. Shi, C.-P. Chen
Department of Materials Engineering
Ming Chi University of Technology
New Taipei City 243, Taiwan
E-mail: cpchen@mail.mcut.edu.tw
Z.-J. Gao, K.-T. Wong
Department of Chemistry
National Taiwan University
Taipei 10617, Taiwan
E-mail: kenwong@ntu.edu.tw
H.-Y. Du
Department of Chemical Engineering
Ming Chi University of Technology
New Taipei City 243, Taiwan
Y.-W. Su, H.-S. Shih
Department of Chemical Engineering
Feng Chia University
Taichung 40724, Taiwan
K.-M. Lee
Department of Chemical and Materials Engineering
Chang Gung University
Taoyuan 33302, Taiwan
H.-H. Hung
Taipei Kuei Shan School
Taipei 112, Taiwan
C. K. Chan
Mechanical Engineering Department
Faculty of Engineering and Quantity Surveying
INTI International University
Nilai, Negeri Sembilan 71800, Malaysia
C.-P. Chen
College of Engineering
Chang Gung University
Taoyuan 33302, Taiwan

The ORCID identification number(s) for the author(s) of this article can be found under https://doi.org/10.1002/adfm.202312819

DOI: 10.1002/adfm.202312819

the range of 1.8–1.9 eV, which differs from the required E_g of ≈1.35 eV for natural sunlight. To effectively harness indoor light, extensive researches have been conducted on multicomponent materials with wider bandgaps or $CsPbI_{3-x}Br_x$ perovskites.[4] Several defect passivation strategies have been employed to enhance the efficiency of indoor perovskite solar cells (iPSCs).[1a,5] As an example, fine-tuning the composition of $CH_3NH_3PbI_{2-x}BrCl_x$ in iPSCs facilitated more efficient carrier transport at the NiO_x/perovskite interface, resulting in an iPCE (indoor photovoltaic conversion efficiency) of 36.2% under 1000 lux fluorescent light.[6] Kim et al., demonstrated an efficient $CH_3NH_3PbI_3$-based iPSC with an indoor power conversion efficiency (iPCE) of 35.5% (Halogen, 1000 lux) via interface engineering.[7] Mai and coworkers showed $Cs_{0.17}FA_{0.83}PbI_{3-x}Br_x$ iPSC with a certified iPCE of 35.36% (1000 lux, 3000 K, LED) by passivating the Br vacancy defects.[4a] Wang et al. introduced an innovative full-dimensional grain boundary stress relief approach, manifesting a durable and flexible α-phase $FAPbI_3$ iPSC with a remarkable PCE of 31.85% under 1062 lux LED illumination (2956 K). Additionally, the utilization of tomato lycopene played a pivotal role in enhancing both the stability and performance of tri-cation iPSCs, resulting in an impressive iPCE exceeding 40% under 1000 lux (Osram L18W/827) lighting conditions.[8] Liu and coworkers reported a guanidinium and 2-(4-methoxyphenyl)ethylamine hydrobromide passivated thick $(FAPbI_3)_{0.97}(MAPbBr_3)_{0.03}$ iPSC with an efficiency of 40.1% (824.5 lux, warm LED).[9] These impressive advances shed the light on the practical approaches of realizing the high-efficiency indoor PSCs. More recently, ion-dipole interactions were demonstrated to achieve an iPCE of 41.2% for $CsPbI_3$ iPSCs.[10] These advancements encourage further exploration and practical applications of iPSC in real-life scenarios.

In pursuit of maximizing the performance of iPSCs to approach theoretical efficiency, it is crucial to concurrently mitigate trap-induced nonradiative carrier recombination within the perovskite and address interface trap state defects, especially when operating under low light-intensity conditions.[1a,b] Enhancing the efficiency of PSCs through interfacial engineering can be achieved by replacing or doping the electron or hole transporting layer (ETL/HTL). This approach offers a straightforward means of improving device performance.[4b,11] A multifunctional interfacial layer can regulate light harvesting, mitigate surface defects, and manage interface hydrophobicity, thereby facilitating effective defect passivation in perovskite materials. In this study, we designed and synthesized coplanar heteroacene dithieno[2,3-d:2′,3′-d′]thieno[3,2-b:3′,2′-b′]dipyrrole (DTPT)-based acceptor-donor-acceptor (A–D–A) derivatives and blended them with phenyl-C_{61}-butyric acid methyl ester (PCBM) as the electron transporting layer (ETL) for iPSCs. The hybrid ETL can effectively address interface defects and manage hydrophobicity, leading to enhanced iPCE and stability in iPSCs. The optimized iPSCs achieved impressive iPCEs of up to 34.1%. Notably, these devices displayed exceptional long-term stability, retaining 87% of their initial iPCE even after a 30-day storage without encapsulation in an environment with 40% relative humidity (RH).

2. Results and Discussion

Lewis base electron donors, such as pyridine, thiophene, and fullerene, have been incorporated to mitigate defects in the perovskite and carrier transport layers. For instance, PCBM is a widely employed material at the interface and as the ETL in PSCs. The strategic control of compatibility and energy level alignment at the perovskite/ETL interface proves to be an effective approach for curtailing trap-induced nonradiative carrier recombination within the perovskite and addressing interfacial trap state defects in iPSCs.[11a] Herein, we synthesize DTPT-cored derivatives with end-capping functional groups either of cyanide, thiophene, carboxyl, and halogen groups to provide specific coordination or electrostatic interactions that might passivate the defects of perovskite. The syntheses of A–D–A-type molecules **DTPTCY, DTPTID2CN**, and **DTPTID2CN2F** are depicted in **Scheme 1**. Detailed synthesis procedure and characterization are shown in Supporting Information, including Figures S1–S10 (Supporting Information). Starting from tetrabromoterthiophene (1),[12] the tandem Buchwald-Hartwig coupling reaction with 2-hexyloctyl amine afforded the branched alkyl chain-substituted N-fused heteropentacene core (2) with a moderate yield of 46%. The electron-rich coplanar core (2) was readily converted to dialdehyde (3) by Vilsmeier-Haack formylation in a good yield of 92%. The aldehyde (3) then underwent a Knöevenagel reaction with 2-methyl-4H-chromen-4-ylidene)malononitrile (CY), 2-(3-oxo-2,3dihydro-1H-inden-1-ylidene)malononitrile (ID2CN), and 2-(5,6-difluoro3-oxo-2,3-dihydro-1H-inden-1-ylidene)malononitrile (ID2CN2F), respectively, to afford the target molecules **DTPTCY** (33%), **DTPTID2CN** (36%), and **DTPTID2CN2F** (40%). The thermogravimetric analysis (TGA) was utilized to investigate the thermal properties of **DTPTCY, DTPTID2CN**, and **DTPTID2CN2F**, as indicated in **Table 1**. All the molecules displayed exceptional thermal stability, with decomposition temperatures (T_d, 5% weight loss) of 371 °C for **DTPTCY**, 339 °C for **DTPTID2CN**, and 324 °C for **DTPTID2CN2F**, respectively.

The UV/Vis absorption spectra of **DTPT** derivatives in chlorobenzene are displayed in Figure S11a (Supporting Information). The maximum absorption peaks and absorption onsets wavelength ($\lambda_{max}/\lambda_{onset}$) of **DTPTCY**, **DTPTID2CN**, and **DTPTID2CN2F** are located at 665/733, 743/793, and 755/807 nm, with corresponding extinction coefficient (ε) of 1.58×10^5, 1.84×10^5, and 9.19×10^4 M^{-1} cm^{-1}, respectively. Each of the **DTPT** derivatives displayed a shoulder peak indicative of their π-π interactions. Notably, the shoulder peaks observed in **DTPTID2CN** and **DTPTID2CN2F** are more pronounced compared to that of **DTPTCY**. This suggests a higher degree of pre-aggregation in **DTPTID2CN** and **DTPTID2CN2F**, potentially affecting their dispersibility due to stronger intermolecular interactions. Figure S11b (Supporting Information) shows the absorption spectra of the neat films of **DTPT** derivatives, while the λ_{onset} of **DTPTCY**, **DTPTID2CN**, and **DTPTID2CN2F** neat films is located at 887, 938, and 935 nm, respectively. By comparison with the absorption spectrum in the solution, the film of **DTPTCY**, **DTPTID2CN**, and **DTPTID2CN2F** present a different redshift of λ_{onset} to be 154,

K.-T. Wong
Institute of Atomic and Molecular Science
Academia Sinica
Taipei 10617, Taiwan

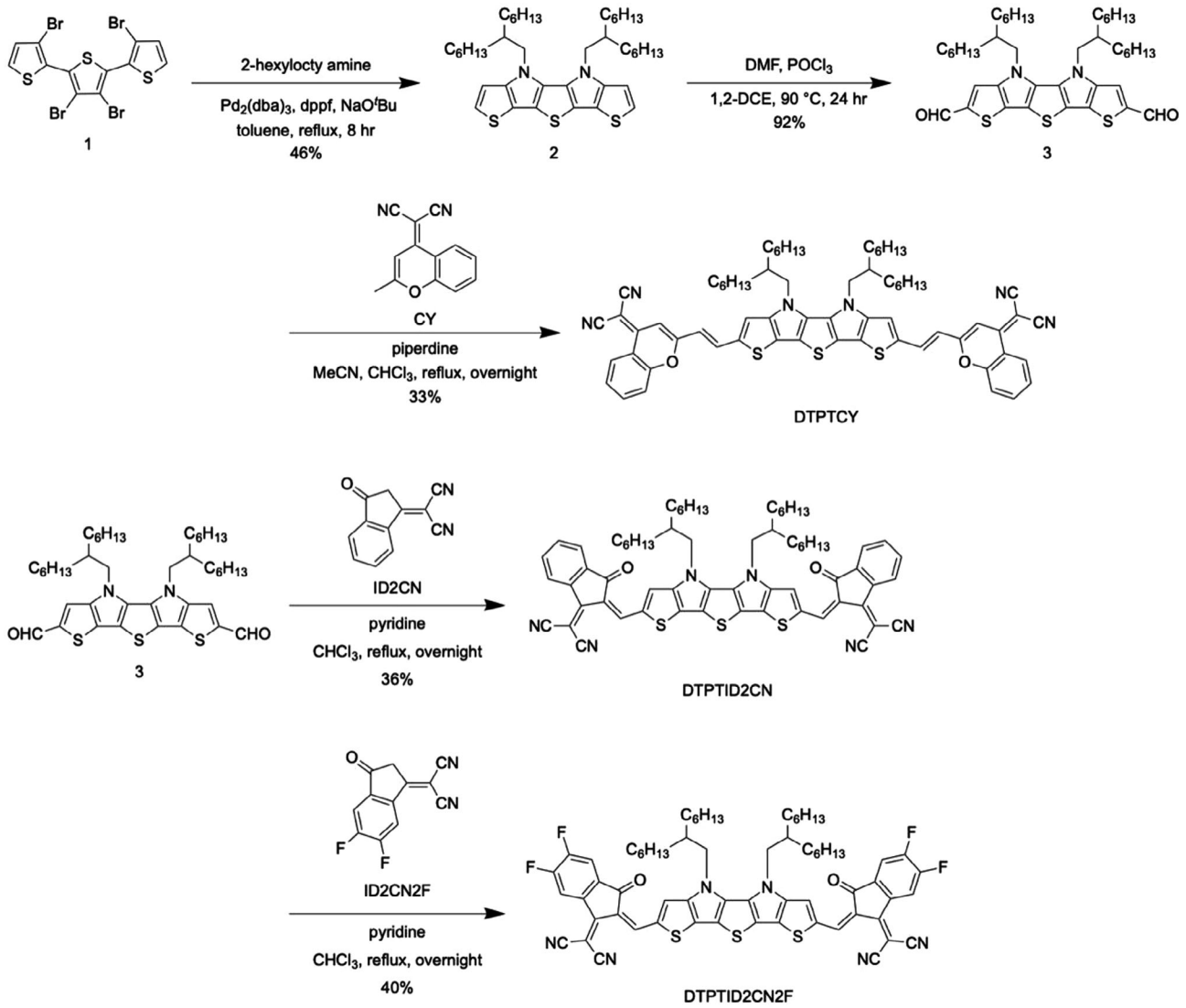

Scheme 1. Synthetic routes for new A-D-A type molecules **DTPTCY**, **DTPTID2CN**, and **DTPTID2CN2F**.

145, and 128 nm, respectively. **DTPTCY** exhibiting a significant redshift than **DTPTID2CN** and **DTPTID2CN2F** implies the experience of strongest intermolecular interactions during the film formation. Furthermore, the absorption of **DTPT** derivatives covers the red to near-infrared region, with comparatively lower absorption in the visible spectrum. This characteristic makes them a promising choice as ETL for PSCs. The electrochemical characteristics of **DTPT** derivatives were investigated by cyclic voltammetry (CV). By referencing the ferrocene/ferrocenium (Fc/Fc^+) redox couple, the corresponding energy levels of the highest occupied molecular orbitals (HOMOs) and lowest unoccupied molecular orbitals (LUMOs) were calculated based on the onsets of the oxidation and reduction potentials. These results are summarized in Table 1. The HOMO/LUMO energy levels of

Table 1. Photophysical and Electrochemical Properties of **DTPTCY**, **DTPTID2CN**, and **DTPTID2CN2F**.

Molecule	$\lambda_{max}/\lambda_{onset}$ [a] [nm]	ε [M^{-1} cm^{-1}] [a]	HOMO [eV] [b,c]	LUMO [eV] [b,d]	T_d [d] [°C] [e]
DTPTCY	665/733	158 000	−5.06	−3.37	371
DTPTIDCN	743/793	184 000	−5.31	−3.75	339
DTPTID2CN2F	755/807	91 900	−5.40	−3.86	324

[a] Measured in chlorobenzene solutions; [b] Measured in CH_2Cl_2 solutions with 0.1 M TBAPF6 as a supporting electrolyte; [c] Measured in THF with 0.1 M TBAP as a supporting electrolyte; [d] Calculated from cyclic voltammetry using Fc/Fc+ (−4.8 eV in vacuum) as a reference electrode; [e] Temperature corresponding to 5% weight loss obtained from TGA under N2 at a heating rate of 10 °C min^{-1}.

DTPTCY, **DTPTID2CN**, and **DTPTID2CN2F** are −5.06/−3.37, −5.31/−3.75, and −5.40/−3.86 eV, respectively. Among these derivatives, **DTPTCY** exhibits a higher LUMO energy level than **DTPTID2CN**, primarily due to the weaker electron-withdrawing properties of the cyanide group. In contrast, **DTPTID2CN2F** attains a lower LUMO energy level, thanks to the incorporation of electron-withdrawing fluorine atoms. Previous studies have indicated that by adjusting the blend ratio, it is possible to readily modulate the energy level of the ETL blend film, placing it within the range of the individual ETLs' energy levels.[13] It is worth noting that the higher energy level of **DTPTCY** offers a wider scope for energy level adjustments when blended with PCBM. Grazing-incidence wide-angle X-ray scattering (GIWAXS) was employed to investigate the molecular packing of **DTPT** derivatives in neat films. Figure S12 (Supporting Information) displays both the 2D and 1D GIWAXS patterns and profiles. In the case of **DTPTCY**, it exhibits an edge-on orientation with a (010) peak observed at 1.82 $Å^{-1}$ (corresponding to a d-spacing of 3.45 Å) in the in-plane (IP) direction. Additionally, there are several strong lamellar peaks at 1.27, 0.84, and 0.42 $Å^{-1}$ in the out-of-plane (OP) direction, indicating a high degree of molecular ordering in the film. **DTPTID2CN** exhibits a similar profile, with an IP (010) peak at 1.82 $Å^{-1}$ (d = 3.45 Å) and several OP lamellar peaks at 1.17, 0.78, and 0.39 $Å^{-1}$. On the other hand, **DTPTID2CN2F** features a lower (010) peak at 1.73 $Å^{-1}$ (d = 3.45 Å) and an OP lamellar peak at 0.33 $Å^{-1}$ (d = 19.04 Å). Notably, **DTPTCY** and **DTPTID2CN**, with higher diffraction intensity, indicate strong molecular packing behavior, which is in line with their observed redshifts in UV-Vis absorption spectra. The structure of the electron-only device comprised of glass/indium tin oxide (ITO)/ZnO/**DTPT** derivatives/PFN-Br/Ag was employed to measure the space charge limited current (SCLC) density curves for **DTPT** derivatives, as depicted in Figure S13 (Supporting Information). The electron mobility (μ_e) of the device was subsequently determined using the following equation

$$J = \frac{9\varepsilon_0\varepsilon_r\mu V^2}{8L^3} \quad (1)$$

where ε_0, ε_r, and L are the relative dielectric constant, the permittivity of free space, and the thickness of **DTPT** derivatives, respectively. The μ_e of **DTPTCY**, **DTPTID2CN**, and **DTPTID2CN2F** samples was found to be 0.81, 0.32 and 0.23×10^{-4} cm^2 V^{-1} s^{-1}, respectively. Among these materials, **DTPTCY** demonstrates a higher μ_e compared to the others, making it the most promising candidate for use as an ETL in PSCs.

Considering the need to adjust the energy level alignment at the perovskite/ETL interface and enhance carrier transport within the ETL, **DTPTCY** was initially selected as the modifier due to its higher LUMO energy level. The p-i-n-type iPSCs were fabricated with the following structure: glass/indium tin oxide (ITO)/NiO_x (30 nm)/ $CH_3NH_3PbI_3$ ($MAPbI_3$)/PCBM, both with and without **DTPTCY**, followed by bathocuproine (BCP, 5 nm)/Ag (100 nm) as shown in **Figure 1a**.[2b,14] The $MAPbI_3$ was deposited from a concentration of 0.8 M in blend solvent (DMF:DMSO = 4:1, v/v) to give a thickness of 300 nm which was suitable for the application of iPVs. Detail fabrication conditions are shown in SI. Due to the interface-related issues, the PSC with **DTPTCY** alone as the ETL exhibited unsatisfactory performance. The blend ratio of the ETL consisting of PCBM and **DTPTCY**, as well as the post-annealing temperature, were examined as these factors have the potential to impact the performance of the PSC. Under 1 sun (AM 1.5 G, 100 mW cm^{-2}), the PCE of PSCs (i.e., PCBM-based PSCs is the control device for comparison) was 13.5 ± 0.8% with a short-circuit current density (J_{SC}) of 18.7 ± 0.6 mA cm^{-2}, an open-circuit voltage (V_{OC}) 1.04 ± 0.02 V and a fill factor(FF) of 69.5 ± 2.5%, as shown in Figure 1b and **Table 2**. Figure S14a and Table S1 (Supporting Information) provide an overview of the device performance of PSCs with various PCBM:**DTPTCY** blend ratios under 1-sun illumination conditions. The PCEs of PSCs with varying blend ratios of PCBM to **DTPTCY**, including 1:0.001, 1:0.01, 1:0.025, and 1:0.05, were measured to be 13.6%, 13.4%, 14.6%, and 11.8%, respectively. Notably, when the **DTPTCY** content is extremely low, particularly at blend ratios of 1:0.001 and 1:0.01, the device performance remains almost unchanged compared to the pristine devices. However, the highest performance was achieved at a blend ratio of 1:0.025. Beyond this optimal ratio, when the **DTPTCY** content exceeds 1:0.05, it resulted in a decline of device performance, consistent with the findings reported in the literature.[11a] Figure S14b and Table S2 (Supporting Information) present the device performance data for PSCs based on a PCBM:**DTPTCY**(1:0.025) blend at varying fabrication temperatures under 1 sun illumination. At ETL fabrication temperatures of 25, 60, 90, and 120 °C, the corresponding PCEs of the PSCs were determined to be 14.6%, 14.7%, 16.8%, and 14.3%, respectively. The observed trend indicates that higher ETL fabrication temperatures result in a notable enhancement in device performance, particularly in terms of J_{SC} and V_{OC}. This suggests that the elevated fabrication temperatures may lead to improved miscibility between PCBM and **DTPTCY**, ultimately maximizing device performance. The optimized PCE of 90 °C **DTPTCY**-based PSCs were 15.9 ± 0.7% with a J_{SC} of 19.0 ± 0.8 mA cm^{-2}, a V_{OC} 1.07 ± 0.01 V and an FF of 78.4 ± 4.0%, as shown in Figure 1b and Table 2. **DTPTCY**-based PSCs exhibited a remarkable increase in PCE, exhibiting an ≈17% enhancement when compared to the control PSCs with PCBM only. This notable improvement can be attributed to a substantial boost in the FF, complemented by the slight increases in both J_{SC} and V_{OC}. As suggested in the previous report,[11a,15] the observed improvement can be attributed to the blended ETL enhancing transport properties and reducing recombination losses. These factors will be further discussed in the following sections. Figure S14c,d (Supporting Information) show the hysteresis curves (delay time: 0.05 s) of the PCBM- and PCBM:**DTPTCY**-based PSCs, corresponding hysteresis index (HI) to be 0.029 and 0.013, respectively. The observation of PCBM:**DTPTCY**-based PSCs having a smaller HI implies that the introduction of **DTPTCY** may contribute to defect passivation in the surface of perovskite layer. Moreover, we conducted stability measurements by maintaining the bias at 0.84 and 0.86 V for PCBM- and PCBM:**DTPTCY**-based PSCs over a duration of 55 s, as illustrated in Figure S15 (Supporting Information). The stabilized efficiencies at the maximum power point for PCBM- and PCBM:**DTPTCY**-based PSCs are 12.2% and 16.0%, respectively. Figure 1c displays the external quantum efficiency (EQE) spectra of PCBM- and PCBM:**DTPTCY**-based PSCs. Then, the calculated values of EQE–J_{SC} of PCBM- and PCBM:**DTPTCY**-based

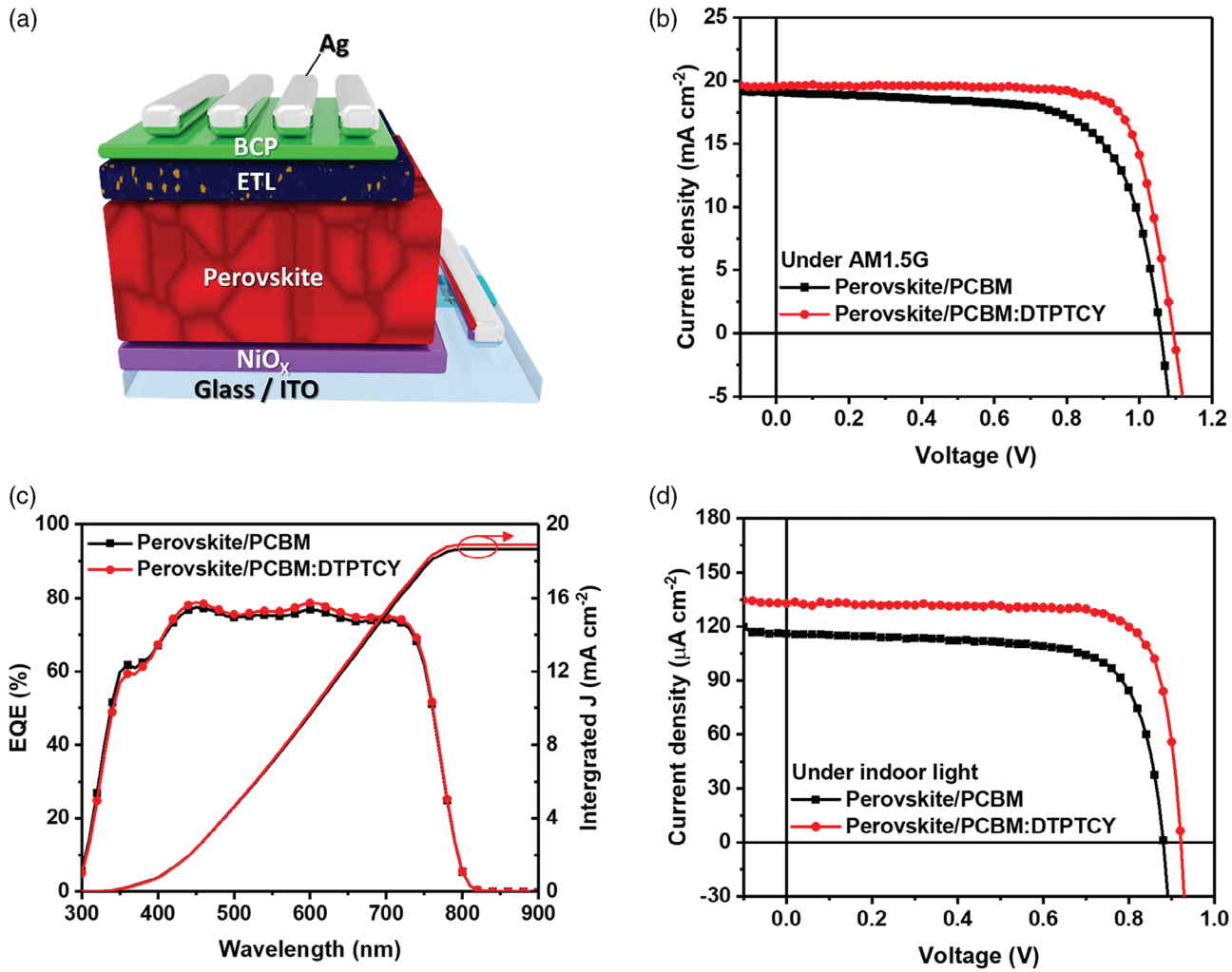

Figure 1. a) The p-i-n PSC device structure in this study. b) *J–V* characteristics under AM1.5G, c) EQE spectra, and d) *J–V* characteristics under indoor light of PCBM- and PCBM:**DTPTCY**-based PSCs.

PSCs are 18.67 and 18.93 mA cm^{-2}, respectively. There are only small mismatches in the EQE responses when compared to the values of J_{SC} obtained from the J-V curves. A similar optimization strategy was employed to assess the impact of **DTPTID2CN** and **DTPTID2CN2F**, and the optimal device performance is shown in Figure S14e and Table S3 (Supporting Information). The PCE for PCBM:**DTPTID2CN**-based PSC is 15.4%, and 10.0% for PCBM:**DTPTID2CN2F**-based PSC. These PCE values are lower than the PCBM:**DTPTCY**-based PSCs.

A 4100 K fluorescent lamp (TL84, European shop fluorescent) was utilized as the light source, and the corresponding emission spectrum is shown in Figure S16 (Supporting Information).[16] Referring to literature,[4a] the power density of indoor light illuminance is generally from 180 to 900 μW cm^{-2}, corresponding the luminance from 200 lux to 1000 lux. Here, the power density of TL84 ranges from 59.4 to 284.4 μW cm^{-2}, corresponding the luminance from 200 lux to 1000 lux, after correction. Figure S17a and Table S4 (Supporting Information) presents the device

Table 2. Device performance of the PSCs.

ETL	Illumination	J_{SC} [mA cm^{-2}]	V_{OC} [V]	FF [%]	PCE [%]	PCE_{best} [%]
PCBM	AM1.5G	18.7 ± 0.6	1.04 ± 0.02	69.5 ± 2.5	13.5 ± 0.8	14.9
PCBM:DTPTCY	100 mW cm^{-2}	19.0 ± 0.8	1.07 ± 0.01	78.4 ± 4.0	15.9 ± 0.7	16.8

ETL	Illumination	P_{in} [μW cm^{-2}]	J_{SC} [μA cm^{-2}]	V_{OC} [V]	FF [%]	iPCE [%]	$iPCE_{best}$ [%]	P_{out} [μW cm^{-2}]
PCBM	TL84	284.4	113.9 ± 1.7	0.86 ± 0.02	72.4 ± 2.3	25.0 ± 1.1	26.7	71.1 ± 3.2
PCBM:DTPTCY	1000 lux		129.5 ± 4.4	0.92 ± 0.01	78.9 ± 2.2	33.1 ± 1.0	34.1	94.0 ± 2.7

performance of PCBM-based PSCs under various light intensities. The iPCE of PCBM-based PSCs under 200, 400, 600, 800, and 1000 lux were measured at 22.7%, 21.8%, 23.2%, 23.9%, and 26.7%, respectively, while the iPCE is increased upon increasing the light intensity. The best average iPCE of 25.0 ± 1.1% was observed under 1000 lux, with a J_{SC} of 113.9 ± 1.7 μA cm^{-2}, a V_{OC} 0.86 ± 0.02 V, and an FF of 72.4 ± 2.3%, as shown in Figure 1d and Table 2. The iPCE of PCBM:**DTPTCY**-based PSCs recorded under 200, 400, 600, and 800 lux are 32.6%, 33.8%, 32.7% and 33.1% (Figure S17b and Table S5, Supporting Information), respectively. Moreover, the PCBM:**DTPTCY**-based PSCs were also assessed under 1000 lux, resulting in an iPCE of 33.1 ± 1.0% (with the best iPCE of 34.1%), with a J_{SC} of 129.5 ± 4.4 μA cm^{-2}, a V_{OC} 0.92 ± 0.01 V, and an FF of 78.9 ± 2.2%. It is worth highlighting that the enhancement in iPCE is ≈32% when compared to the control PCBM-based PSCs. This increase is more substantial than the observed PCE enhancement under AM 1.5G, suggesting that this improvement strategy is particularly well-suited for the development of iPV. Remarkably, the iPCE of PCBM:**DTPTCY**-based PSCs remains at ≈30%, even when the light intensity drops below 500 lux. In contrast, the control device exhibits a significant decline in performance as the light intensity decreases. Based on our understanding, the performance of PSCs involves the filling of traps within the PSCs prior to charge transport. Therefore, trap density can have a significant impact on device performance, especially when measured under indoor lighting conditions, which correspond to lower charge densities. In this context, we anticipated that **DTPTCY** could effectively mitigate surface defects that could otherwise lead to undesirable trap-assisted recombination, ultimately resulting in enhanced device performance even under light intensities below 500 lux. Figure S17c,d (Supporting Information) present the hysteresis curves (with a delay time of 0.05 s) for both PCBM- and PCBM:**DTPTCY**-based PSCs under 1000 lux illumination. The corresponding indoor hysteresis index (iHI) values were found to be 0.085 for PCBM-based PSCs and 0.035 for PCBM:**DTPTCY**-based PSCs. Compared with HI under AM1.5G, iHI is slightly higher, attributed to the fact that devices operating at lower charge densities, such as those in indoor lighting, tend to be more sensitive to defects within the device, potentially resulting in increased hysteresis.[3b] The **DTPTCY**-blended device exhibits a lower iHI compared to the control device, suggesting that **DTPTCY** likely plays a pivotal role in passivating defects within the device. The PSCs that incorporated **DTPTID2CN** or **DTPTID2CN2F** were also evaluated under 1000 lux, resulting in iPCE value of 28.6% and 28.1%, respectively (Figure S17e and Table S6, Supporting Information). Table S7 (Supporting Information) presents data from previous reports on iPV based on PSCs. It is observed that $MAPbI_3$-based PSCs achieved impressive iPCEs ranging from ≈25.1% to 37.2% under 1000 lux of fluorescent or LED lighting. However, the $CsPbI_{3-x}Br_x$ and multicomponent PSCs reached a breakthrough iPCE ≈40%. Moreover, the iPCEs of most PSCs tend to decrease as the light intensity decreases, with the iPCE ratio ($iPCE/iPCE_{1000lux}$) under illumination <400 lux ranging from 0.91 to 0.55. Conversely, PSCs based on PCBM:**DTPTCY** displays a significant iPCE/iPCE1000 lux ratio of 0.96 when operating at 200 lux. This observation suggests that the inclusion of **DTPTCY** ensures that these PSCs maintain exceptional iPCE performance even when exposed to reduced light intensities, making them highly suitable for indoor applications. When considering IoT applications, it is important to note that lower-intensity light sources, like 200 lux (typical of living room lighting) or 500 lux (common in office environments), are more prevalent in the everyday human surroundings.

Here, GIWAXS was employed to assess alterations in the molecular packing of PCBM after the introduction of **DTPT** derivatives, as illustrated in Figure S18 (Supporting Information). The typical (010) peak of the pristine PCBM neat film was observed at 1.41 $Å^{-1}$(d = 4.45 Å), which is consistent with our previous report.[17] Upon the introduction of **DTPT** derivatives, all blend films exhibited a similar profile to that of the PCBM neat film. This similarity can be attributed to the relatively low quantity of **DTPT** derivatives added to the blends. However, the location of (010) peaks were observed with a slight shift at 1.37 $Å^{-1}$ (4.58 Å), 1.33 $Å^{-1}$ (4.73 Å), and 1.33 $Å^{-1}$ (4.73 Å) when blending with **DTPTCY**, **DTPTID2CN**, and **DTPTID2CN2F**, respectively. Upon blending with **DTPTID2CN** or **DTPTID2CN2F**, a noticeable increase in the π-stacking distance was observed. In contrast, when blended with **DTPTCY**, the increase in π-stacking distance was comparatively smaller. This larger π-stacking distance could potentially impact electron mobility and subsequently lead to a less pronounced improvement in device performance. To further investigate the primary role of the **DTPT** derivatives, **DTPTCY** was selected as a representative compound for further analysis in the subsequent sections. The field emission scanning electron microscopy (FE-SEM) was applied to record changes in morphology, as shown in Figure S19 (Supporting Information). The samples of $MAPbI_3$/PCBM and $MAPbI_3$/PCBM:**DPTPCY** exhibited a similar perovskite morphology, implying that the impact on perovskite morphology via the ETL can be ignored. We studied the effects of morphology and contact surface potential (CPD) that affecting the performance of devices through the atomic force microscopy (AFM) and Kelvin probe force microscope (KPFM) measurements. Figure S20 (Supporting Information) depicts the surface morphology of perovskite/PCBM and perovskite/PCBM:**DTPTCY**. The root mean square (RMS) surface roughness of perovskite films with PCBM and PCBM:**DTPTCY** as ETLs was measured at 0.86 and 0.43 nm, respectively. This data indicates a reduction in surface roughness for the ETL incorporating **DTPTCY**. Generally, a smoother interface is associated with fewer defects that improve the exciton extraction at the interface. Therefore, one of the reasons for the enhancement in device performance can be attributed to the smoother surface observed in the presence of **DTPTCY**. Additionally, a distinct fibril-like structure on the surface of the film incorporating **DTPTCY** was observed, which may correspond to the crystalline structure of **DTPTCY** moieties. This unique morphology feature can facilitate electron transport within the ETL and thus improve overall performance. The CPD is equivalent to the surface potential voltage and can be described as the difference in the work functions between the sample and tip, divided by the negative electron charge. Here, we use the same KPFM measurement parameters in different perovskite/ETLs structures and take ITO as a standard reference for the CPD comparison. Schematic illustrations for different perovskite/ETLs layers structures are show in **Figure 2a**. From right to left are perovskite without ETL, with PCBM and with PCBM: **DTPTCY**, respectively. The fresh sample surface is scratched to create ITO and layer structures interface for the following discussion. Figure 2b

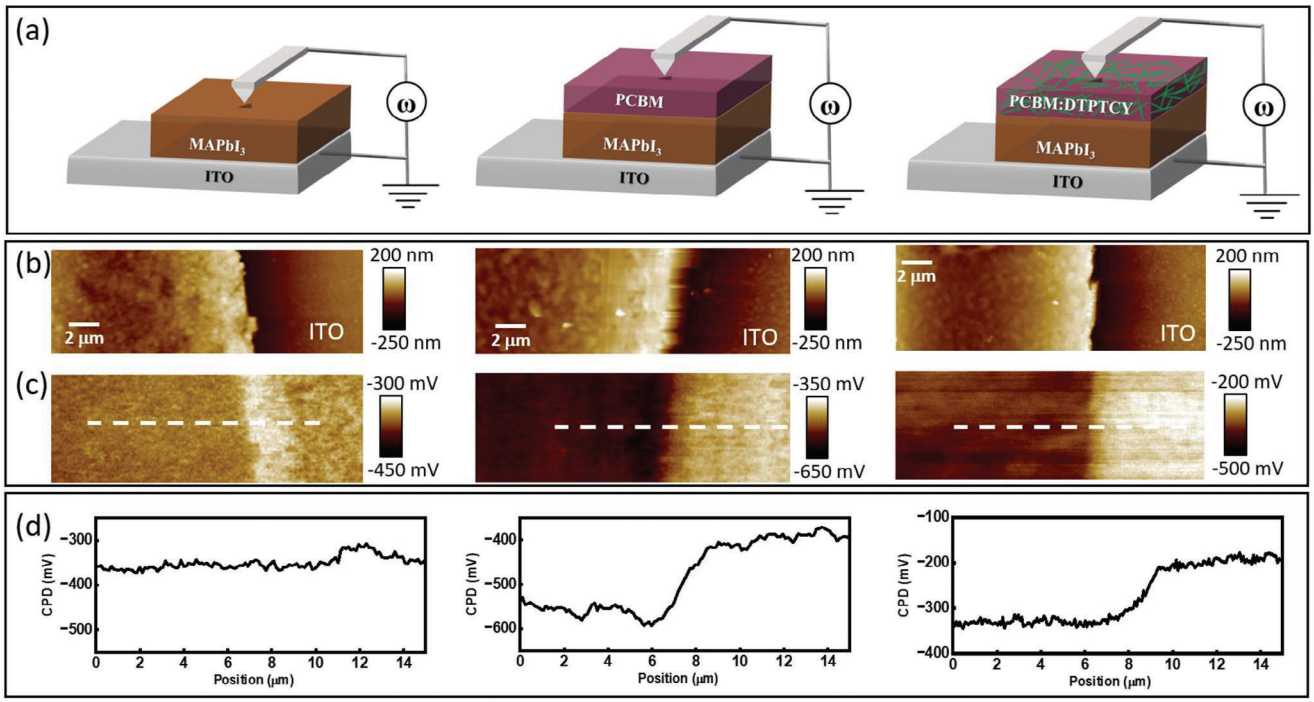

Figure 2. AFM-KPFM characterizations. a) Schematic illustrations for different ETLs /perovskite layers structures. From right to left are perovskite without ETL, with PCBM and with PCBM: **DTPTCY**, respectively. b) Topography and c) CPD maps of perovskite without ETL, with PCBM and with PCBM: **DTPTCY**, respectively. d) CPD line profiles corresponding to the lines marked in (c).

show the surface morphology of different perovskite/ETLs layers structures. The thickness of barely $MAPbI_3$, with PCBM and with PCBM:**DTPTCY** is 300, 380 and 380 nm respectively (Figure S21, Supporting Information). To verify the existence of such potential dip in the transport layer, Figure 2c shows the surface potential of different perovskite/ETLs layers structures. We compare this energetic disorder difference between with ITO of barely $MAPbI_3$, PCBM and PCBM:**DTPTCY** by the CPD difference (ΔCPD). Figure 2d shows the CPD line profiles at different perovskite/ETLs layers structures. The ΔCPD with ITO of barely $MAPbI_3$, PCBM and PCBM:**DTPTCY** are 50, 160 and 120 mV, respectively. Among these samples, $MAPbI_3$ exhibits the lowest ΔCPD, while the highest ΔCPD was obtained after depositing a PCBM layer, indicating the presence of a barrier between perovskite and PCBM. However, the $MAPbI_3$/PCBM:**DTPTCY** sample displays a lower ΔCPD than $MAPbI_3$/PCBM, suggesting that the energy levels of ETL have been adjusted. Moreover, a lower barrier was observed between perovskite and PCBM:**DTPTCY**, which may facilitate energy level alignment, ensuring efficient charge transport. Then, ultraviolet photoelectron spectrometer (UPS) was used to investigate the change in energy level, as shown in Figure S22a–c (Supporting Information), where the work function was determined by using the relationship WF (eV) = 21.22 – $E_{cut\text{-}off}$. The valence band maximum levels (E_{VBM}) was determined by the band edge; the conduction band maximum (E_{CBM}) was determined by using the bandgap of corresponding films.[15] The results of UPS are summarized in a schematic illustration, as shown in Figure S22b (Supporting Information). Among them, similar E_{VBM} and E_{CBM} were observed in the perovskite, regardless of the presence or absence of PCBM, while the main difference was from the WF. However, a deeper energy level was identified in the perovskite films when PCBM:**DTPTCY** was present, promoting favorable energy level alignment between the perovskite and the electrode. This observation confirms that **DTPTCY** has the ability to fine-tune the energy levels, ensuring efficient charge transport and potentially suppressing unwanted recombination during the charge transfer processes.

X-ray photoelectron spectroscopy (XPS) was employed to investigate the interactions between **DTPTCY** and the perovskite. In **Figure 3a**, the high-resolution XPS spectra of the S2p binding energies are displayed for the **DTPTCY** sample and the perovskite/PCBM:**DTPTCY** sample. The signals in the S2p spectrum are divided into two peaks at 163.3 and 164.5 eV, corresponding to the $S2p_{3/2}$ and $S2p_{1/2}$ orbitals, respectively. These peaks can be attributed to the presence of thiophene from **DTPTCY**.[18] Similar signals were also observed in the S2p spectrum of the perovskite/PCBM:**DTPTCY** sample, indicating that **DTPTCY** is indeed present in the ETL. Importantly, a slight shift between the two samples was detected, implying the possibility of passivation or interaction between **DTPTCY** and the perovskite. Figure 3b shows the Pb4f binding energies for the samples of perovskite, perovskite/PCBM, and perovskite/PCBM:**DTPTCY**. The signals in the Pb4f spectrum can be classified into two peaks at 141.4 and 136.8 eV, corresponding to the $Pb4f_{5/2}$ and $Pb4f_{7/2}$ orbitals, respectively, which are typical peaks associated with the perovskite material.[19] Comparing the peak locations, highly similar profiles were observed between the sample of perovskite and perovskite/PCBM. However, significant shifts toward higher binding energies were

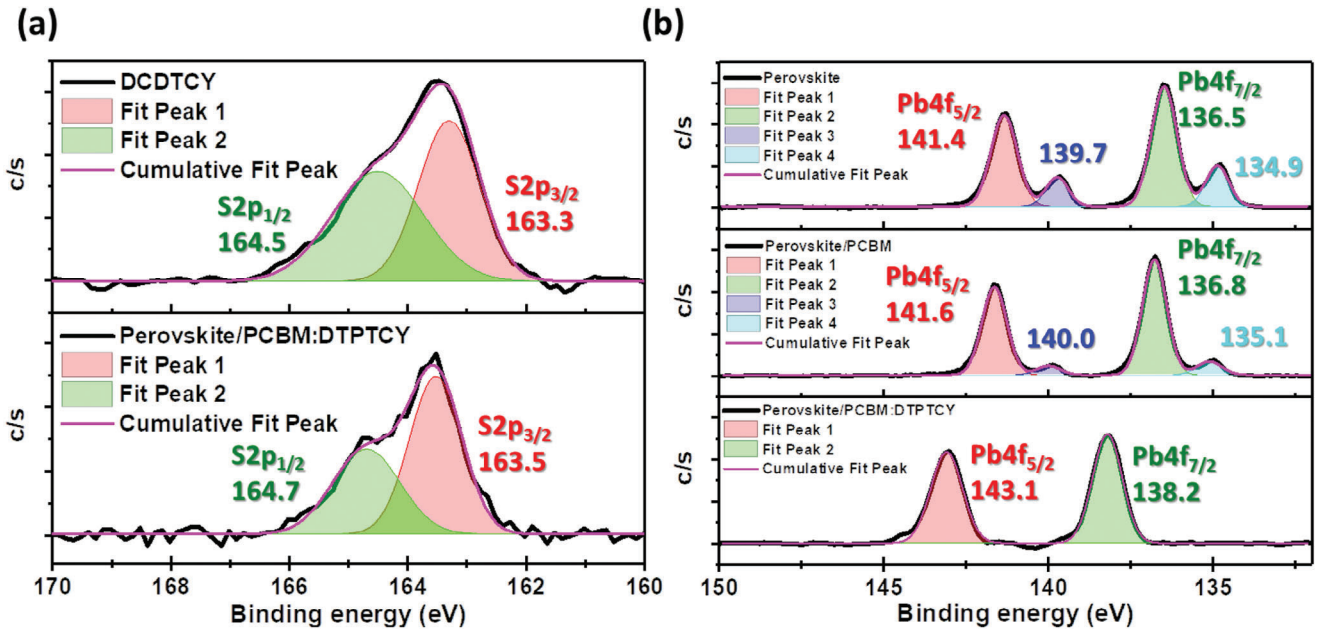

Figure 3. High-resolution XPS spectra of the a) S2p and b) Pb4f 1s binding energies of perovskite films prepared with/without ETL.

observed in the sample of perovskite/PCBM:**DTPTCY**, confirming the presence of coordination interactions between **DTPTCY** and Pb^{2+}.[20] Moreover, in the samples of perovskite, additional peaks were observed at ≈135 and 140 eV, corresponding to the signals of Pb^0. This implies that a portion of Pb^{2+} ions may have underwent reduction.[19] Even when covering the perovskite with PCBM (i.e., perovskite/PCBM), the signals of Pb^0 are still detectable but with lower intensity. However, the signals of Pb^0 disappear in the sample of perovskite/PCBM:**DTPTCY**, indicating that the stronger coordination interactions inhibit the reduction of Pb^{2+} ions. Fourier-transform infrared spectroscopy (FTIR) was employed to record the interaction between the ETL and the perovskite, as depicted in Figure S23 (Supporting Information). The spectrum of the PCBM neat film exhibited signals of C═O, CH_2, C—C, and C—O, consistent with the literature.[21] The **DTPTCY** neat film displayed signals of CH_2, C≡N, C═C, and C—O, similar to other A–D–A molecules.[22] The blend film of PCBM:**DTPTCY** with a blend ratio of 1:0.025 exhibited a curve similar to the PCBM neat film. As the blend ratio increased to 1:1, the signals of **DTPTCY** became more pronounced without disappearance or shift, implying the absence of a chemical reaction between PCBM and **DTPTCY**. The spectra of the $MAPbI_3$ neat film showed signals of N-H and CH_3, consistent with the literature.[23] Comparing the spectra of $MAPbI_3$, $MAPbI_3$/PCBM, and $MAPbI_3$/PCBM:**DTPTCY**, the signals of C═O and C≡N were observed in the spectra of $MAPbI_3$/PCBM and $MAPbI_3$/PCBM:**DTPTCY**, confirming the presence of PCBM and **DTPTCY**. However, the chemical shift was challenging to observe due to the low amount of **DTPTCY** in the ETL. Thus, the film of $MAPbI_3$/**DTPTCY** was employed as a model sample to evaluate the interaction. Compared with the **DTPTCY** neat film, the signals of C≡N and C–O bonds on the **DTPTCY** slightly shifted from 2198 to 2200 cm^{-1} and 1139 to 1136 cm^{-1}, respectively, implying the pathway of passivation and coordination. Thus, the introduction of **DTPTCY** can effectively reduce the surface defects of the perovskite, resulting in the inhibition of unwanted recombination and energy loss, ultimately improving the device performance. Photoluminescence (PL) and time-resolved photoluminescence (TRPL) spectroscopy were employed to investigate the characteristics of photo-exciton generation and transfer process. Samples of perovskite, perovskite/PCBM, and perovskite/PCBM:**DTPTCY** were deposited onto glass substrates. Excitation light with a wavelength of 550 nm was introduced from the glass side to ensure that the emission originated from the perovskite. Figure S24a (Supporting Information) displays the PL spectra, where the perovskite neat film exhibits a strong emission centered at 770 nm. However, significant quenching behavior was observed in both the samples of perovskite/PCBM and perovskite/PCBM:**DTPTCY**. This result indicates the effective extraction of electrons from the perovskite. Notably, a slight shift in emission was observed when comparing the samples of perovskite/PCBM and perovskite/PCBM:**DTPTCY**. This shift could be attributed to the coordination interaction observed in the XPS results. Figure S24b (Supporting Information) shows the TRPL spectra, which were recorded using a peak emission at 478 nm and fitted using a bi-exponential model. The fitted data, including the fractions of the fast (τ_1) and slow (τ_2) decay times representing quenching via trap-mediated nonradiative recombination and radiative recombination of free charge carriers, respectively, are summarized in Table S8 (Supporting Information).[14,24] The values of τ_1 / τ_2 / $\tau_{average}$ for the perovskite, perovskite/PCBM, and perovskite/PCBM:**DTPTCY** were 5.46/52.03/13.52, 2.78/11.26/2.94, and 1.95/9.17/1.95 ns, respectively. Among them, the perovskite neat film presents the highest value of τ_2 because there is no ETL to extract the charge, resulting in serious recombination within the perovskite layer. When the perovskite incorporates PCBM as the ETL, the free charge is quickly extracted, resulting in a

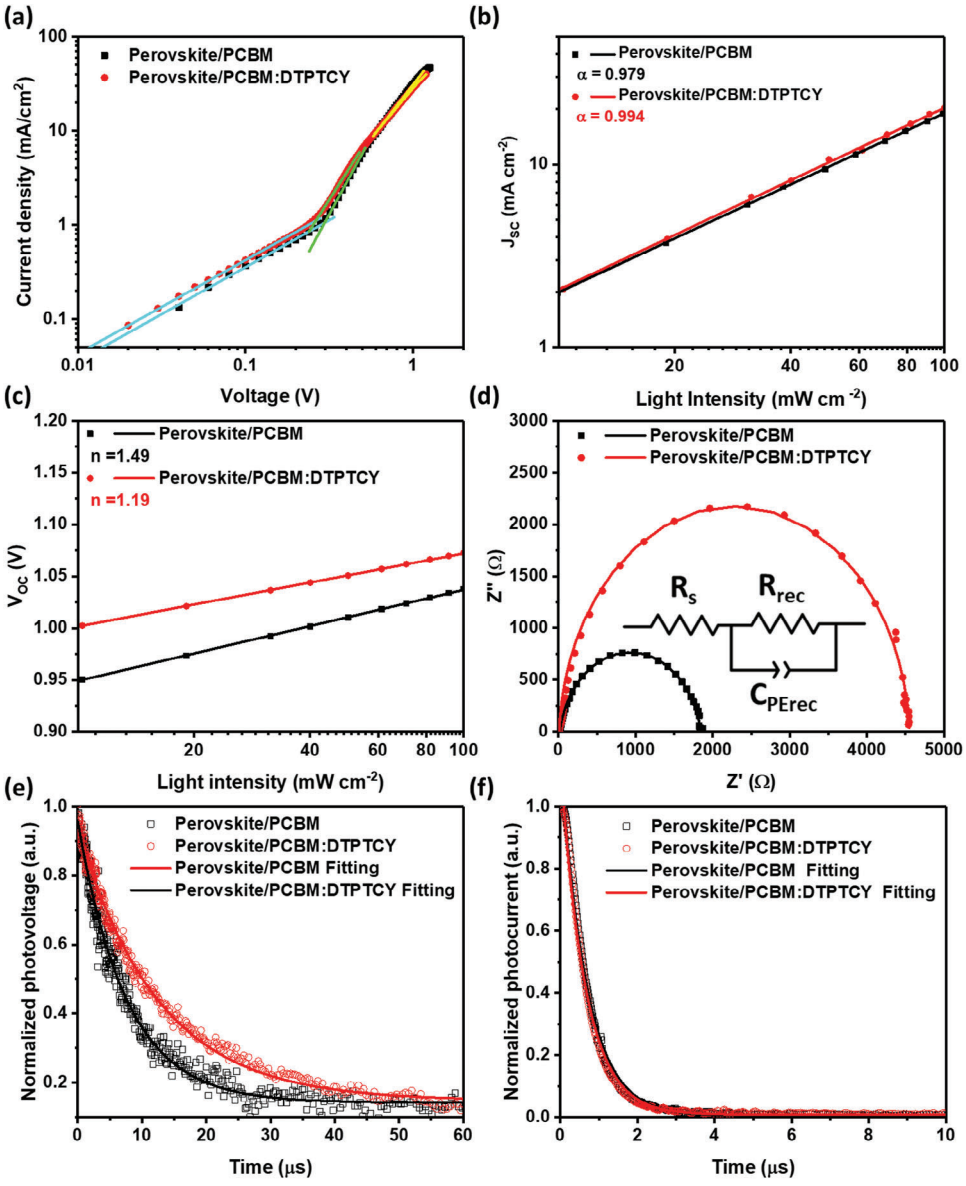

Figure 4. a) SCLC electron only curves b) J_{SC}- light intensity plots, c) V_{OC}- light intensity plots, d) EIS plots, e) TPV plots, f) TPC plots of devices.

significant decrease in τ_2 and A_2. However, when the perovskite incorporated with the PCBM:**DTPTCY**-based ETL, it displays the lowest values of τ_2 and A_2, suggesting that charge transfer to the ETL is more effective due to the presence of **DTPTCY**. This improvement could be attributed to the suitable energy level alignment between the perovskite and PCBM:**DTPTCY**.

An electron-only device (ITO/SnO_2/perovskite/ETLs/Ag) was fabricated to investigate how the ETL affects the electron mobility and trap density of the PSCs, as determined from their SCLC density curves.[2a] The trap density from the *J*–*V* plots on a log–log scale was estimated. The trap density was calculated from the trap-filled-limit voltage (V_{TFL}):

$$V_{TFL} = \frac{e n_{trp} L^2}{2\varepsilon\varepsilon_0} \quad (2)$$

where e (C) is the elementary charge, L (m) is the thickness of the active layer, ε (F m^{-1}) is the relative dielectric constant of perovskite, ε_0 (F m^{-1}) is the vacuum permittivity, and n_{trap} (cm^{-3}) is the trapping state density. **Figure** 4a displays the *J*–*V* curve of the electron-only devices. The calculated trap densities for the PCBM and PCBM:**DTPTCY** samples were 1.16 and 1.03 × 10^{16} cm^{-3}, respectively. Consequently, the electron trapping state density is reduced in the presence of **DTPTCY**, which aligns with the results obtained from XPS. Furthermore, the electron mobility (μ_e) of the devices was calculated. The μ_e for the devices with PCBM and PCBM:**DTPTCY** are 2.67 and 2.70 × 10^{-4} cm^2 V^{-1} s^{-1}, respectively. Hence, electron transport within the perovskite becomes more efficient in devices incorporating PCBM:**DTPTCY**, owing to the PCBM:**DTPTCY**-based ETL featuring a suitable energy level alignment that enhances the effective extraction of electrons from the perovskite. The *J*–*V* curves

of PCBM- and PCBM:**DTPTCY**-based PSCs were recorded under various light intensities (P_{light}), and the corresponding J_{SC}–P_{light} and V_{OC}–P_{light} curves were obtained, as shown in Figure 4b,c.[25] The equation $J_{SC} \propto P_{light}^{\alpha}$ was used to fit the J_{SC}–P_{light} curves in order to determine the fitting value of α, which represents the degree of bimolecular recombination (i.e., $\alpha \approx 1$ implies minimal recombination, $\alpha < 1$ implies more recombination). The fitted α values for PCBM- and PCBM:**DTPTCY**-based PSCs are 0.979 and 0.994, respectively, indicating that bimolecular recombination is suppressed by introducing **DTPTCY**. The equation $V_{OC} = (nkT/q)\ \ln(P_{light})$ was used to fit the V_{OC}–P_{light} curves and obtain the fitting value of n, where k is the Boltzmann constant, T is the absolute temperature, and q is the elemental charge. This value of n was used to assess the degree of trap-assisted recombination, where a higher value of n indicates more pronounced trap-assisted recombination. The fitted n values of PCBM- and PCBM:**DTPTCY**-based PSCs are 1.49 and 1.19, respectively. These values suggest that the suppression of the trap-assisted recombination is significantly improved by introducing **DTPTCY**, which is consistent with the results of trap density measurements. We then used electrochemical impedance spectroscopy (EIS) to investigate charge transfer kinetics and the internal resistances of the perovskite/ETL structures to support of the enhancements in iPCE. Figure 4d displays the Nyquist plots of the EIS data collected in the dark. The figure presents well semicircles (symbols: experimental data; solid curves: fitting data) in the determined frequency range. The semicircles in the high-frequency region are related to the values of C and R_{rec}, larger semicircles imply a greater carrier recombination resistance. The R_{rec} of PCBM- and PCBM:**DTPTCY**-based PSCs are 1843 and 4547 Ω, respectively. The result indicates a lower charge recombination rate and smaller dark current of the device with PCBM:**DTPTCY**; this sequence is consistent with the increase of the FF and values of V_{OC}.[2a] Using transient photovoltage (TPV) measurements under V_{OC} conditions and transient photocurrent (TPC) measurements under short-circuit conditions, charge lifetime and charge extraction efficiency was examined, respectively (Figure 4e,f).[2a] As calculated from Figure 3e, the carrier lifetime of the PCBM:**DTPTCY**-based PSCs was measured to be 12.6 µs, which is longer than that in the PCBM-based PSC with a carrier lifetime of 7.6 µs. A longer carrier lifetime indicates the suppression of charge recombination in the PSC. The fitted values from TPC (Figure 4f curves for the PCBM- and PCBM:**DTPTCY**-based PSCs are 0.67 and 0.64 µs, respectively. A shorter extraction time signifies more efficient charge extraction at the ETL interface, which correlates with the increased mobility and appropriate energy level alignment within the PSC. The improvements observed in PCBM:**DTPTCY**-based PSCs, notably in mitigating undesired carrier recombination, trap-assisted recombination and carrier recombination resistance, outperformed other benefits. The effective suppression of trap-assisted recombination has been demonstrated to be pivotal in sustaining high iPV performance under low light intensities.[1a,b]

To affirm the versatility of our hybrid ETL and enhance the indoor performance of the device, we incorporated a wide bandgap (WBG) $Cs_{0.18}FA_{0.82}Pb(I_{0.8}Br_{0.2})_3$ perovskite layer with an energy bandgap of 1.64 eV. This choice precisely aligns with the spectra of indoor lighting, aiming to optimize performance under such conditions.[26] Under AM1.5G illumination, the performance of PCBM derived $Cs_{0.18}FA_{0.82}Pb(I_{0.8}Br_{0.2})_3$ PSCs was 16.5 ± 0.5%, accompanied by a J_{SC} of 18.4 ± 0.9 mA cm^{-2}, a V_{OC} of 1.22 ± 0.01 V, and an FF of 74.2 ± 2.7%, as illustrated in **Figure 5**a and summarized in **Table 3**. When employing PCBM:**DTPTCY** as the ETL, the PCE of WBG-PSCs reached 19.2 ± 0.8%, showcasing a J_{SC} of 19.5 ± 0.6 mA cm^{-2}, a V_{OC} of 1.24 ± 0.01 V, and an FF of 78.9 ± 1.1%. The performance of PCBM:**DTPTCY**-based WBG-PSCs surpassed that of PCBM-based WBG-PSCs, consistent with the results observed in $MAPbI_3$-based PSCs. Figure 5b presented the EQE spectra of PCBM- and PCBM:**DTPTCY**-based WBG-PSCs, with integrated EQE-J_{SC} values of 19.24 and 19.53 mA cm^{-2}, respectively. Under indoor lighting conditions (TL84_1000 lux), the iPCE of PCBM derived WBG-PSCs was 33.2 ± 0.3% (Figure 5c and Table 3). The iPCE of PCBM:**DTPTCY** WBG-PSCs reached 36.7 ± 0.7%, exhibiting a J_{SC} of 131.9 ± 1.0 µA cm^{-2}, a V_{OC} of 1.01 ± 0.01 V, and a FF of 78.0 ± 1.6%. This iPCE was among the highest value on similar-component PSCs (Table S7, Supporting Information). In addition, an LED array was employed to simulate 3000K LED (via an Indoor PV measurement system with Indoor Lighting Simulator (LED Type), CMS-PV102, ITRI, Taiwan) as indoor light for determining the iPCE of PCBM:**DTPTCY**-based WBG-PSCs, and the corresponding emission spectrum is presented in Figure S25 (Supporting Information). Under 3000K LED with 1000 lux, the average iPCE of respective WBG-PSCs reached 39.6 ± 0.4%, accompanied by a J_{SC} of 277.7 ± 1.8 µA cm^{-2}, a V_{OC} of 1.07 ± 0.01 V, and an FF of 79.2 ± 0.5%, with the best iPCE achieving 39.9% (Figure 5d; Table S9, Supporting Information). This superior iPCE exceeded that of PCBM-based WBG-PSCs (iPCE = 34.5 ± 1.1) and stands among the best recent reports (Table S7, Supporting Information).

Ensuring the shelf-life stability of iPVs is quite essential, particularly for their utilization in the IoT. In this context, PSCs based on PCBM and PCBM:**DTPTCY** were stored within an Ar-filled glove box (i.e., as perfect encapsulation). The recorded data and findings are compiled and presented in **Figure 6**a. After storing the PSCs for over 300 days, it was observed that the PCBM-based PSCs retained ≈80% of their original PCEs. In contrast, the PCBM:**DTPTCY**-based PSCs exhibited a remarkable retention of over 95% of their original PCEs. This significant improvement in stability is likely due to the defect passivation properties of **DTPTCY**, which effectively inhibits device degradation over time.[27] In addition, both PSCs were stored within an Ar-filled glove box, while heating at 85 °C, to record the thermal stability, as shown in Figure S26a (Supporting Information). Under thermal stress, the PCBM-based PSCs presented a quick decrease, corresponding to a PCE retention of 50% of their original after 120 h. PCBM:**DTPTCY**-based PSCs provided improved thermal stability, corresponding to a PCE retention of 92% of their original after 216 h. Moreover, both PSCs were stored within an Ar-filled glove box under continuous illumination (100 mW cm^{-2}, LED-HPLS, ENLI technology Co., Taiwan), to evaluate long-term operational stability and photostability, as shown in Figure S26b (Supporting Information). The PCBM- and PCBM:**DTPTCY**-based PSCs retained 51% and 60% of their original PCE after 73 h, respectively. Furthermore, both PSCs were subjected to storage under ambient conditions (40% relative humidity, 25 °C, dark, in air) without any encapsulation, simulating accelerated testing conditions. The results are presented in Figure 6b. Remarkably, when assessing changes in

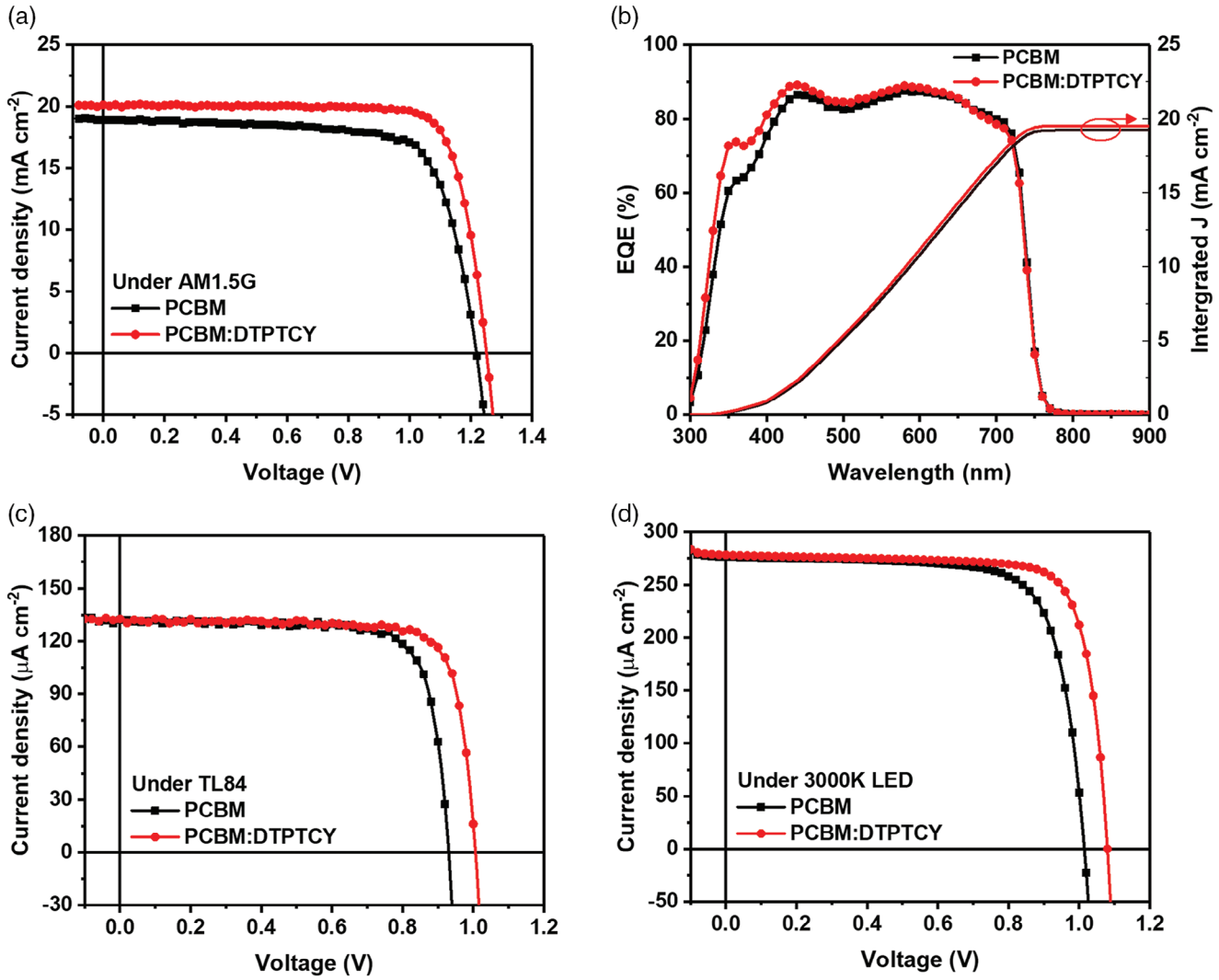

Figure 5. a) *J–V* characteristics under AM1.5G, b) EQE spectra, c) *J–V* characteristics under TL84 and, d) under 3000K LED of PCBM- and PCBM:**DTPTCY**-based WBG-PSCs.

iPCE under indoor light (TL84, 1000 lux), both devices demonstrated impressive stability. After storing for >30 days, the PCBM-based PSCs exhibits a reduction to ≈67% of their initial iPCEs. Conversely, the PCBM:**DTPTCY**-based PSCs retains over 87% of their initial performance, even after 30 days of storage. The notable disparity in air stability could indeed be linked to the hydrophobic properties of the ETL. Water and diiodomethane were employed as probe solvents to measure the contact angle, and Wu's model was applied to compute the surface energy, as shown in Figure S27 and Table S10 (Supporting Information). The water contact angles for perovskite, perovskite/PCBM, and perovskite/PCBM:**DTPTCY** were determined to be 29.05°, 79.18°, and 81.92°, respectively. The highest water contact angle was observed on perovskite/PCBM:**DTPTCY**, indicating a

Table 3. Device performance of the WBG-PSCs.

ETL	Illumination	J_{SC} [mA cm^{-2}]	V_{OC} [V]	FF [%]	PCE [%]	PCE_{best} [%]
PCBM	AM1.5G	18.4 ± 0.9	1.22 ± 0.01	74.2 ± 2.7	16.5 ± 0.5	17.2
PCBM:DTPTCY	100 mW cm^{-2}	19.5 ± 0.6	1.24 ± 0.01	78.9 ± 1.1	19.2 ± 0.8	20.2

ETL	Illumination	P_{in} [μW cm^{-2}]	J_{SC} [μA cm^{-2}]	V_{OC} [V]	FF [%]	iPCE [%]	$iPCE_{best}$ [%]	P_{out} [μW cm^{-2}]
PCBM	TL84	284.4	131.9 ± 0.1	0.90 ± 0.01	77.8 ± 0.9	33.2 ± 0.3	33.4	94.3 ± 0.9
PCBM:DTPTCY	1000 lux		131.9 ± 1.0	1.01 ± 0.01	78.0 ± 1.6	36.7 ± 0.7	37.2	104.3 ± 1.9

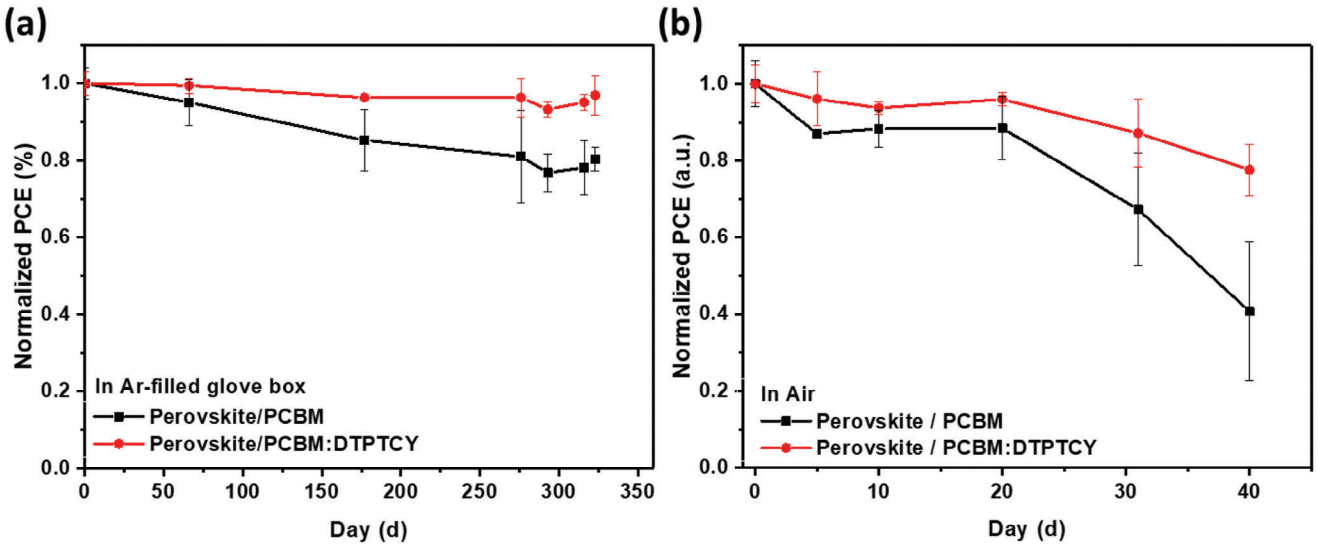

Figure 6. Stabilities of the PSCs measured a) inside a glove box and b) under exposure to ambient air (25 °C, 40% humidity).

more hydrophobic surface compared to the other configurations. The surface energies of perovskite, perovskite/PCBM, and perovskite/PCBM:**DTPTCY** were determined to be 79.50, 55.23, and 51.31 mN m^{-1}, respectively. Perovskite/PCBM:**DTPTCY** exhibits a lower surface energy, which could potentially inhibit the adhesion of H_2O or O_2. Additionally, the presence of defects in the perovskite could create pathways for water infiltration, and the inhibition of defects by DTPTCY might contribute to the enhanced stability of PCBM:DTPTCY-based PSCs.[28]

3. Conclusion

We have undertaken the design, synthesis, and comprehensive characterization of a series of small molecules featuring a central **DTPT** core. These molecules have been blended with PCBM to serve as the ETL, effectively enhancing the performance of PSCs. The incorporation of **DTPTCY** into PCBM enables us to fine-tune the energy levels within the ETL, resulting in a favorable energy level alignment between the perovskite and the ETL. Notably, **DTPTCY** has demonstrated its capability to coordinate with Pb^{2+} ions, effectively preventing the reduction of Pb^{2+} to Pb^0. Within the PCBM:DTPTCY-ETL, a fibril-like structure is formed, significantly enhancing electron mobility. This structure effectively suppresses bimolecular recombination and facilitates shorter extraction times in the device. The reduction in defects and lower trap density within the perovskite layer has a significant impact on device performance, particularly under indoor lighting conditions. PSCs derived from **DTPTCY** have demonstrated an iPCE of up to 34.1% (TL84_1000 lux). Moreover, a comparable improvement was noted in $Cs_{0.18}FA_{0.82}Pb(I_{0.8}Br_{0.2})_3$-based PSCs that integrated the blended ETL, attaining iPCE values of 37.2% and 39.9% under TL84 and 3000K LED lighting conditions, respectively. Furthermore, the PCBM:**DTPTCY**-based ETL effectively addresses interface defects and controls hydrophobicity, resulting in outstanding long-term stability. These devices retain 87% of their initial iPCE even after a 30-day storage period without encapsulation under 40% RH conditions. Our study offers a novel approach to advance high-performance indoor PSCs, particularly in environments with lower light intensity (e.g., 200–500 lux).

Supporting Information

Supporting Information is available from the Wiley Online Library or from the author.

Acknowledgements

B.-H.J., Z.-J.G. and C.-Y. L. contributed equally to this work. The authors thank the National Science and Technology Council of Taiwan (NSTC 112-2113-M-131-001; 111-2221-E-131-018-MY2, 110-2113-M-002-008-MY3) for providing financial support.

Conflict of Interest

The authors declare no conflict of interest.

Data Availability Statement

The data that support the findings of this study are available in the supplementary material of this article.

Keywords

defect passivation, electron transporting layer, N-type, perovskite solar cell

Received: October 17, 2023
Revised: December 12, 2023
Published online:

[1] a) B. T. Muhammad, S. Kar, M. Stephen, W. L. Leong, *Mater. Today Energy* **2022**, *23*, 100907; b) K.-L. Wang, Y.-H. Zhou, Y.-H. Lou, Z.-K. Wang, *Chem. Sci.* **2021**, *12*, 11936; c) C. Polyzoidis, K. Rogdakis, E. Kymakis, *Adv. Energy Mater.* **2021**, *11*, 2101854; d) N. Yan, C. Zhao, S. You, Y. Zhang, W. Li, *Chin. Chem. Lett.* **2019**, *31*, 643.

[2] a) Y.-L. Chiu, C.-W. Li, Y.-H. Kang, C.-W. Lin, C.-W. Lu, C.-P. Chen, Y. J. Chang, *ACS Appl. Mater. Interfaces* **2022**, *14*, 26135; b) S.-C. Lin, T.-H. Cheng, C.-P. Chen, Y.-C. Chen, *Mater. Chem. Phys.* **2022**, *288*, 126385; c) T. Wang, Y. Zhang, W. Kong, L. Qiao, B. Peng, Z. Shen, Q. Han, H. Chen, Z. Yuan, R. Zheng, X. Yang, *Science* **2022**, *377*, 1227; d) Y. An, N. Zhang, Z. Zeng, Y. Cai, W. Jiang, F. Qi, L. Ke, F. R. Lin, S.-W. Tsang, T. Shi, A. K. Y. Jen, H.-L. Yip, *Adv. Mater.* **2023**, 230 6568.

[3] a) Q. Jiang, J. Tong, Y. Xian, R. A. Kerner, S. P. Dunfield, C. Xiao, R. A. Scheidt, D. Kuciauskas, X. Wang, M. P. Hautzinger, R. Tirawat, M. C. Beard, D. P. Fenning, J. J. Berry, B. W. Larson, Y. Yan, K. Zhu, *Nature* **2022**, *611*, 278; b) A. Venkateswararao, J. K. W. Ho, S. K. So, S.-W. Liu, K.-T. Wong, *Mater Sci Eng R Rep* **2020**, *139*, 100517; c) G. K. Grandhi, L. Krishnan Jagadamma, V. Sugathan, B. Al-Anesi, D. Manna, P. Vivo, *Chem. Commun.* **2023**, *59*, 8616; d) Y. Li, T. Nie, X. Ren, Y. Wu, J. Zhang, P. Zhao, Y. Yao, Y. Liu, J. Feng, K. Zhao, W. Zhang, S. Liu, *Adv. Mater.*, 2306870.

[4] a) C. Zhang, C. Liu, Y. Gao, S. Zhu, F. Chen, B. Huang, Y. Xie, Y. Liu, M. Ma, Z. Wang, S. Wu, R. E. I. Schropp, Y. Mai, *Adv. Sci.* **2022**, *9*, e2204138; b) N. Li, A. Feng, X. Guo, J. Wu, S. Xie, Q. Lin, X. Jiang, Y. Liu, Z. Chen, X. Tao, *Adv. Energy Mater.* **2022**, *12*, 2103241; c) Y. Tong, A. Najar, L. Wang, L. Liu, M. Du, J. Yang, J. Li, K. Wang, S. F. Liu, *Adv. Sci.* **2022**, *9*, e2105085.

[5] S. Jiang, Y. Bai, Z. Xu, F. Wang, L. Xia, Y. Yang, C. Li, Z. '. Tan, *Small Methods* **2022**, *6*, 2200624.

[6] R. Cheng, C.-C. Chung, H. Zhang, F. Liu, W.-T. Wang, Z. Zhou, S. Wang, A. B. Djurisic, S.-P. Feng, *Adv. Energy Mater.* **2019**, *9*, 1901980.

[7] S. J. Shin, G. Alosaimi, M. J. Choi, M. H. Ann, G. G. Jeon, J. Seidel, J. Kim, J. S. Yun, J. H. Kim, *ACS Appl. Energy Mater.* **2022**, *5*, 13234.

[8] C. Dong, X.-M. Li, C. Ma, W.-F. Yang, J.-J. Cao, F. Igbari, Z.-K. Wang, L.-S. Liao, *Adv. Funct. Mater.* **2021**, *31*, 2011242.

[9] X. He, J. Chen, X. Ren, L. Zhang, Y. Liu, J. Feng, J. Fang, K. Zhao, S. F. Liu, *Adv. Mater.* **2021**, *33*, 2100770.

[10] K.-L. Wang, H. Lu, M. Li, C.-H. Chen, D.-B. Zhang, J. Chen, J.-J. Wu, Y.-H. Zhou, X.-Q. Wang, Z.-H. Su, Y.-R. Shi, Q.-S. Tian, Y.-X. Ni, X.-Y. Gao, S. M. Zakeeruddin, M. Grätzel, Z.-K. Wang, L.-S. Liao, *Adv. Mater.* **2023**, *35*, 2210106.

[11] a) Z. Cheng, C. Gao, J. Song, D. Ding, Y. Chen, J. Wang, D. Zhang, L. Chen, X. Wang, Z. Yang, F. Liu, H. Liu, W. Shen, *ACS Appl. Mater. Interfaces* **2021**, *13*, 40778; b) H.-H. Huang, T.-A. Yang, L.-Y. Su, C.-H. Chen, Y.-T. Chen, D. Ghosh, K.-F. Lin, S. Tretiak, C.-C. Chueh, W. Nie, H. Tsai, L. Wang, *ACS Mater. Lett.* **2023**, *5*, 1384; c) H. Zhang, C. Zhao, J. Yao, W. C. H. Choy, *Angew. Chem., Int. Ed.* **2023**, *62*, e202219307.

[12] C.-L. Chung, C.-H. Chen, C.-H. Tsai, K.-T. Wong, *Org. Electron.* **2015**, *18*, 8.

[13] J. Gao, X. Ma, C. Xu, X. Wang, J. H. Son, S. Y. Jeong, Y. Zhang, C. Zhang, K. Wang, L. Niu, J. Zhang, H. Y. Woo, J. Zhang, F. Zhang, *Chem. Eng. J.* **2022**, *428*, 129276.

[14] H.-L. Hsu, B.-H. Jiang, J.-M. Lan, C.-H. Wu, R.-J. Jeng, C.-P. Chen, *Adv. Electron. Mater.* **2021**, *7*, 2000870.

[15] J. Ho Lee, I. Su Jin, J. Woong Jung, *Chem. Eng. J.* **2021**, *420*, 129678.

[16] C.-Y. Liao, Y. Chen, C.-C. Lee, G. Wang, N.-W. Teng, C.-H. Lee, W.-L. Li, Y.-K. Chen, C.-H. Li, H.-L. Ho, P. H.-S. Tan, B. Wang, Y.-C. Huang, R. M. Young, M. R. Wasielewski, T. J. Marks, Y.-M. Chang, A. Facchetti, *Joule* **2020**, *4*, 189.

[17] J.-H. Lu, B.-H. Jiang, F.-C. Hsiao, Y.-C. Peng, Y.-W. Su, Y.-R. Lin, T.-H. Tsai, M.-N. Shiu, C.-Y. Lin, Y.-T. Fang, C.-P. Chen, *Chem. Eng. J.* **2022**, *437*, 135327.

[18] M. H. Elsayed, B.-H. Jiang, Y.-P. Wang, P.-Y. Chang, Y.-C. Chiu, R.-J. Jeng, H.-H. Chou, C.-P. Chen, *J. Mater. Chem. A* **2021**, *9*, 9780.

[19] S. Ning, S. Zhang, J. Sun, C. Li, J. Zheng, Y. M. Khalifa, S. Zhou, J. Cao, Y. Wu, *ACS Appl. Mater. Interfaces* **2020**, *12*, 43705.

[20] a) M. Pegu, A. Ghaderian, S. Ahmad, S. Kazim, *ChemPlusChem* **2022**, *87*, 202200021; b) M. Li, H. Li, Q. Zhuang, D. He, B. Liu, C. Chen, B. Zhang, T. Pauporté, Z. Zang, J. Chen, *Angew. Chem., Int. Ed.* **2022**, *61*, e202206914; c) S. Tang, Y. Peng, Z. Zhu, J. Zong, L. Zhao, L. Yu, R. Chen, M. Li, *J. Phys. Chem. Lett.* **2022**, *13*, 5116; d) Z. Zhao, J. Wu, Y.-Z. Zheng, N. Li, X. Li, X. Tao, *ACS Catal.* **2019**, *9*, 8144.

[21] D. Qu, T. Guo, J. Zhang, Z. Deng, Z. Zhang, R. Zhao, X. Liu, Z. Hu, L. Huang, Y. Zhu, *Appl. Phys. Lett.* **2021**, *119*, 143902.

[22] J. Guo, Y. Wu, R. Sun, W. Wang, J. Guo, Q. Wu, X. Tang, C. Sun, Z. Luo, K. Chang, Z. Zhang, J. Yuan, T. Li, W. Tang, E. Zhou, Z. Xiao, L. Ding, Y. Zou, X. Zhan, C. Yang, Z. Li, C. J. Brabec, Y. Li, J. Min, *J. Mater. Chem. A* **2019**, *7*, 25088.

[23] a) Y. Xu, Y. Huang, H. Zhong, W. Li, D. Cao, C. Zhang, H. Bao, Z. Guo, L. Wan, X. Zhang, X. Zhang, Y. Li, X. Wang, D. Eder, S. Wang, *ACS Appl. Energy Mater.* **2021**, *4*, 11314; b) A. Jancik Prochazkova, M. C. Scharber, C. Yumusak, J. Jancik, J. Másilko, O. Brüggemann, M. Weiter, N. S. Sariciftci, J. Krajcovic, Y. Salinas, A. Kovalenko, *Sci. Rep.* **2020**, *10*, 15720.

[24] a) C.-H. Chiang, M. K. Nazeeruddin, M. Grätzel, C.-G. Wu, *Energy Environ. Sci.* **2017**, *10*, 808; b) H.-L. Hsu, H.-T. Hsiao, T.-Y. Juang, B.-H. Jiang, S.-C. Chen, R.-J. Jeng, C.-P. Chen, *Adv. Energy Mater.* **2018**, *8*, 1802323.

[25] a) B.-H. Jiang, Y.-C. You, D.-W. Lin, C.-P. Chen, K.-T. Wong, *ACS Appl. Energy Mater.* **2022**, *5*, 15423; b) B.-H. Jiang, Y.-P. Wang, C.-Y. Liao, Y.-M. Chang, Y.-W. Su, R.-J. Jeng, C.-P. Chen, *ACS Appl. Mater. Interfaces* **2021**, *13*, 1076.

[26] a) H. Bi, J. Liu, Z. Zhang, L. Wang, R. Beresneviciute, D. Tavgeniene, G. Kapil, C. Ding, A. K. Baranwal, S. R. Sahamir, Y. Sanehira, H. Segawa, S. Grigalevicius, Q. Shen, S. Hayase, *ACS Energy Lett.* **2023**, *8*, 3852; b) Y. Ou, H. Huang, H. Shi, Z. Li, Z. Chen, M. Mateen, Z. Lu, D. Chi, S. Huang, *Chem. Eng. J.* **2023**, *469*, 143860.

[27] M.-H. Li, T.-G. Sun, J.-Y. Shao, Y.-D. Wang, J.-S. Hu, Y.-W. Zhong, *Nano Energy* **2021**, *79*, 105462.

[28] W. Chi, S. K. Banerjee, *Chem. Mater.* **2021**, *33*, 4269.